LAUTECH Journal of Engineering and Technology 20 (2) 2026: 14-29
10.36108/laujet/6202.02.0290

Effect of the Heat-Affected Zone on the Mechanical Properties and Microstructure of TIG-Welded Cast Iron/Aluminum Alloy Joints

***[1]Adesina A. O., [2]Bello K. A., [3]Mudashiru L. O., [1]Oyetunde R. A.**

[1]*Department of Mechanical Engineering, Yaba College of Technology, Yaba, Nigeria*

[2]*Department of Mechanical Engineering, Federal University, Oye Ekiti, Nigeria*

[3]*Department of Mechanical Engineering, Ladoke Akintola University of Technology, Ogbomoso, Nigeria*

Article Info

Article history:

Received: Mar. 25, 2026
Revised: May 12, 2026
Accepted: May 17, 2026

Keywords:

Heat-affected Zone,
TIG Welding,
Gray Cast Iron,
Aluminum Alloy 6063,
Mechanical Properties,
Dissimilar-metal Joints.

Corresponding Author:
oluwoleadesina9@gmail.com

ABSTRACT

The welding of Gray Cast Iron (ASTM A48M) and Aluminum Alloy 6063 dissimilar metals using Tungsten Inert Gas (TIG) welding remains a current challenge in engineering due to the thermal cycling in the heat- affected zone (HAZ) that causes microstructural transformation, which controls the joint's mechanical properties. In this research, the TIG-welded sample (200 mm x 200 mm x 30 mm) was prepared using 240 V and 90 A, and then post- weld cooled by three methods: natural air cooling, oil quenching and water quenching. Hardness (Vickers), impact toughness (Charpy) and tensile testing were conducted on the weldment, HAZ and base metal with SEM micrography and SEM/EDX elemental analysis. Maximum weldment hardness was achieved with oil quenching in both cast iron (310.7 HV) and Al 6063 (146.8 HV) but maximum HAZ hardness in cast iron (292.0 HV) was obtained with water quenching. Natural cooling produced the highest tensile strength and impact toughness for both cast iron (424.5 MPa) and Al 6063 (110.2 MPa). SEM analysis confirmed martensitic structures in the water-quenched cast iron HAZ, a bainitic matrix under oil quenching, and an equilibrium ferrite-pearlite-graphite microstructure under natural cooling. SEM/EDX mapping confirmed Mg2Si precipitate formation in Al 6063 and showed no significant Fe-Al interdiffusion at the fusion interface. These results provide practical guidance for post-weld cooling strategy selection in dissimilar-metal TIG welding applications.

INTRODUCTION

Welding of cast iron and aluminum alloy (dissimilar-metal) is becoming essential in automotive powertrain, brake-system, and lightweight structural systems where optimisation of thermal conductivity, weight reduction, and wear resistance is required in a single assembly (Okafor *et al*., 2022; Messler, 2004). The increased use of aluminum alloy 6063 as a structural extrusion material, as well as the long service life of gray cast iron as the engine blocks and cylinder heads, results in common engineering situations where the two materials need to be reliably joined (Ramji *et al*., 2021; Ning *et al*., 2023).

Tungsten Inert Gas (TIG) welding, or Gas Tungsten Arc Welding (GTAW), is popular in such joints because of its tight heat control and clean inert-atmosphere shielding, and its ability to work with a wide range of materials (Kou, 2003; Lancaster, 1999). The process, however, forms a complex thermal cycle, which results in three different microstructural regions, including the fusion zone (weldment), the heat-affected zone (HAZ), and the unaffected base metal. The HAZ is also very sensitive, as it is subjected to quick thermal cycling without melting, which causes coarsening of the grains, formation of phases, and accumulation of residual stress that often dictate the location of failure of the whole joint (Gharibshahiyan *et al*., 2011; Lippold, 2023). The cooling plan after welding has a conclusive impact on HAZ microstructure and properties. The diffusion-controlled phase transformations are inhibited by rapid quenching, and the harder but more brittle microstructures are favored, whereas natural air cooling permits longer diffusion and microstructural recovery at the expense of reduced hardness (Porter *et al*., 2009; Cao *et al*., 2025).In the case of gray cast iron, in particular, the cooling rate dictates the change between stable graphite flakes and the metastable white-iron (ledeburite) phase, and its far-reaching implications on cooling determine the distribution and fineness of the Mg_2Si strengthening precipitates that determine the hardness and tensile behavior (Callister and Rethwisch, 2018; Balasubramanian *et al*., 2008). Previous literature has described single materials during TIG welding. Baghel *et al*. (2022) and Cui *et al*. (2015) showed that the process parameters are critical in controlling HAZ width and hardness distribution in high-strength steels. According to Balasubramanian *et al*. (2008), grain growth and tensile strength reduction in aluminum alloy weldments are directly related to heat input. Zhang *et al*. (2024) conducted a general review of the weldability of cast iron and determined the cooling rate as the most significant variable that determines the quality of the joints. However, the synergistic, cumulative influence of three commercially useful quenching media on the entire mechanical property profile hardness, impact toughness, and tensile strength throughout all three areas of a Gray Cast Iron / Al 6063 dissimilar joint has not been reported in the past.

MATERIALS AND METHODS

Materials

Gray Cast Iron (ASTM A48M) and Aluminum Alloy 6063 were selected as base materials. Plate specimens measuring 200 mm × 200 mm × 30 mm were machined to size. Chemical compositions confirmed by spectrometric analysis are presented in Tables 1 and 2.

Table 1: Chemical composition of Gray Cast Iron ASTM A48M (wt. %)

Element	Fe	C	Si	Mn	P	S	Cu	Mo
Mean	93.96	3.32	1.90	0.32	0.01	0.01	0.20	0.12
SD	0.03	0.03	0.10	0.50	0.01	0.01	0.002	0.004

Table 2: Chemical composition of Aluminum Alloy 6063 (wt. %)

Element	Al	Si	Fe	Cu	Mn	Mg	Zn
Mean	98.29	0.22	0.21	0.29	0.10	0.83	0.02
SD	0.02	0.00	0.10	0.50	0.01	0.01	0.007

Welding Procedure and Post-Weld Cooling

TIG (GTAW) welding was performed at 240 V and 90 A. Joint edges were cleaned before welding. Nine specimens per material (three per test type) were produced under each of three post-weld quenching conditions: (i) natural air cooling, (ii) oil quenching, and (iii) water quenching, yielding a 2 × 3 × 3 factorial experimental design (material × cooling medium × test zone).

Mechanical Testing

Vickers hardness was measured across the weldment, HAZ, and base metal. Charpy V-notch impact tests were conducted at room temperature per ISO 148-1. Uniaxial tensile tests were performed on a universal testing machine. Three replicate measurements were averaged per condition.

Microstructural Characterization

Cross-sections were prepared by grinding, polishing, and etching: Nital (2% HNO_3 in ethanol) for cast iron; NaOH aqueous solution at 70 °C for aluminum. Optical micrographs and SEM images were acquired across all zones to correlate microstructure with mechanical properties.

RESULTS

Vickers Hardness

Table 3 summarizes Vickers hardness results. In the weldment zone, oil quenching produced the highest hardness for both cast iron (310.7 HV) and aluminum alloy (146.8 HV), attributable to the formation of fine martensitic/bainitic phases under rapid cooling. Water quenching maximized HAZ hardness in cast iron (292.0 HV). Natural cooling yielded the lowest hardness across all zones for both materials. Cast iron hardness values were 90-100% higher than aluminum equivalents in every zone.

Figure 1 and Figure 2 (Cast iron and Al 6063 weldment zones, respectively) present the hardness distributions graphically, which reveal the regularity of the ranking of the cooling conditions over the entire range of measurement. This high hardness in oil and water quenching can be attributed to inhibition of diffusion-controlled transformations: fast extraction of heat hinders diffusion of carbon in cast iron, allowing martensite and bainite to form instead of the softer ferrite-pearlite products that form on slow cooling (Porter *et al*., 2009). The rapid cooling in Al 6063 maintains a greater amount of fine Mg_2Si precipitates in the matrix that inhibit dislocation movement to increase hardness (Callister and Rethwisch, 2018). These processes are also well-founded on the basis of classical solid-state transformation theory and are in agreement with previous experimental results on related alloy systems (Gharibshahiyan *et al*., 2011; Balasubramanian *et al*., 2008). Practically, the oil quenching hardness benefit (310.7 HV in cast iron weldment) renders this cooling strategy especially appropriate in wear-sensitive service applications, where tribological performance is directly dictated by surface hardness, e.g., brake components and gear surfaces.

Table 3: Vickers hardness (HV) by zone and cooling condition

Zone	Material	Natural	Oil	Water
Weldment	Cast Iron	259.8	310.7	274.4
Weldment	Al 6063	117.0	146.8	126.5
HAZ	Cast Iron	247.1	288.0	292.0
HAZ	Al 6063	88.8	132.8	123.3
Base	Cast Iron	225.3	-	-
Base	Al 6063	93.7	-	-

Note: Hardness of base metals is only considered for natural cooling since the base metal specimens were not also put in post-weld quenching conditions; those entries that are marked with a - have not been applied to unaffected base metal.

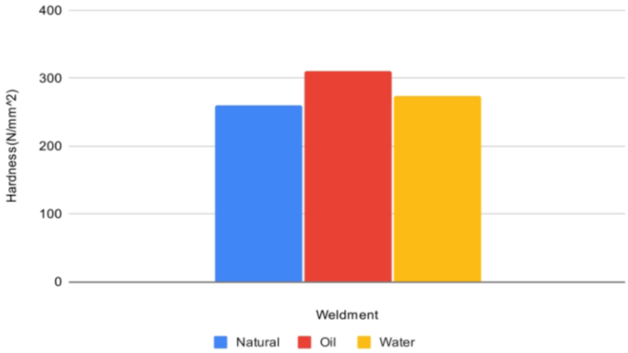

Figure 1: Hardness of Gray Cast Iron weldment zone

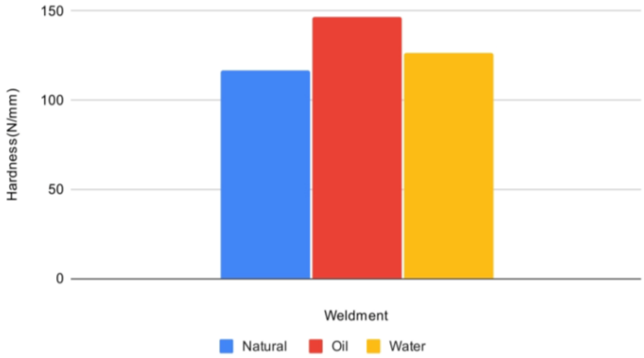

Figure 2: Hardness of Aluminum Alloy 6063 weldment zone

Charpy Impact Toughness

Table 4 shows the inverse trend to hardness: natural cooling consistently produced the highest impact energy. Cast iron weldment absorbed 18.20 J under natural cooling versus 15.32 J under water quenching, a 19% reduction. The base metal (19.14 J) outperformed all welded conditions, confirming that the thermal cycle inherently reduces toughness.

Aluminum alloy impact values were 35-45% lower than cast iron across equivalent conditions. Figures 3 and 4 show the influence of the energy distributions of the cast iron and Al 6063 weldment areas, respectively, and it confirms the negative correlation between the cooling rate and the absorbed energy. The loss in impact toughness during rapid quenching can be explained by the development of martensitic and bainitic phases in cast iron, which are brittle in nature and the high residual stresses and dislocation density in Al 6063, that minimizes the ability of the materials to absorb plastic energy before a propagating crack (Lancaster, 1999; Lippold, 2015). This is a long-standing phenomenon in metallurgy and welding literature: the Hall-Petch hardness-yield strength enhancement that comes with rapid cooling hardens and increases hardness and yield strength but, at the same time, lowers fracture toughness by restricting dislocation movement (Porter *et al*., 2009). This has the practical implication that structures loaded dynamically or under impact, as in automotive chassis joints or pressure vessel components, should be post-weld cooled by natural air cooling to maintain sufficient toughness margins and prevent brittle fracture in service.

Table 4: Charpy impact energy (J) by zone and cooling condition

Zone	Material	Natural	Oil	Water
Weldment	Cast Iron	18.20	16.86	15.32
Weldment	Al 6063	12.70	11.66	10.94
HAZ	Cast Iron	16.43	14.71	15.11
HAZ	Al 6063	10.32	9.23	9.65
Base	Cast Iron	19.14	-	-
Base	Al 6063	12.01	-	-

Note: Base metal impact energy values were only considered when the cooling is natural and are marked with a- when conditions did not apply to unaffected base metal specimens not quenched post-weld.

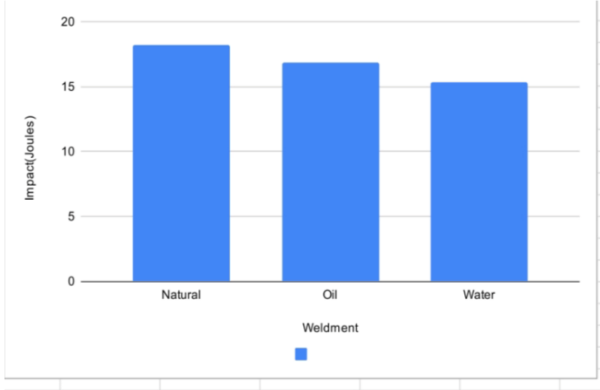

Figure 3: Impact energy of Gray Cast Iron weldment zone

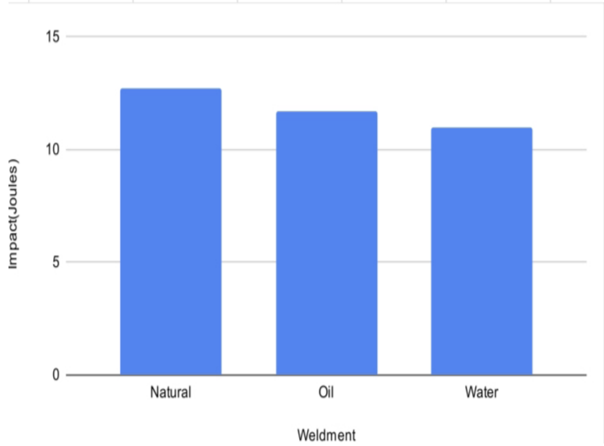

Figure 4: Impact energy of Aluminum Alloy 6063 weldment zone

Tensile Properties

Table 5 confirms that natural cooling preserves the highest UTS in both materials. Cast iron UTS under natural cooling (424.5 MPa) was 2.5× the oil-quenched value (166.7 MPa), a remarkable reduction attributed to residual-stress-induced crack nucleation from martensitic phases. For aluminum alloy, the UTS range was narrower (85.8-110.2 MPa), with natural cooling again superior. Figure 5 and Figure 6 show the tensile strength profiles of cast iron and Al 6063 weldment specimens under the three conditions of cooling that visually confirms the high performance of natural cooling in maintaining tensile load-bearing capacity. This is attributed to the dramatic loss in cast iron UTS under oil quenching (166.7 MPa, a 61% decrease compared to natural cooling), which is due to the formation of brittle martensite, as well as the accumulation of internal residual stresses during rapid cooling, which both contribute to pre-existing crack initiation sites that prematurely fail under tensile loading at stresses that are significantly lower than the theoretical. The smaller UTS range (85.8-110.2 MPa) in Al 6063 is a result of the naturally greater ductility of the face-centred cubic matrix relative to cast iron, which is more tolerant of residual stress and heterogeneity of the microstructure without catastrophic loss of strength. These results are in harmony with the fact that post-weld residual stress management is equally crucial as microstructural control in ensuring tensile integrity of joints (Messler, 2004). Where tensile strength is needed either to support load, like in the case of load-bearing brackets or frame joints, or due to the need to contain pressure, like in the case of pressure-containing parts, natural air cooling is highly encouraged as the preferred post-weld treatment.

Table 5: Tensile properties of weldment specimens

Material	Condition	UTS (MPa)	E (MPa)	Force (N)
Cast Iron	Natural	424.5	1688	12369
Cast Iron	Water	342.4	1251	10190
Cast Iron	Oil	166.7	1071	5014
Al 6063	Natural	110.2	460	6877
Al 6063	Oil	94.4	381	6117
Al 6063	Water	85.8	1199	5709

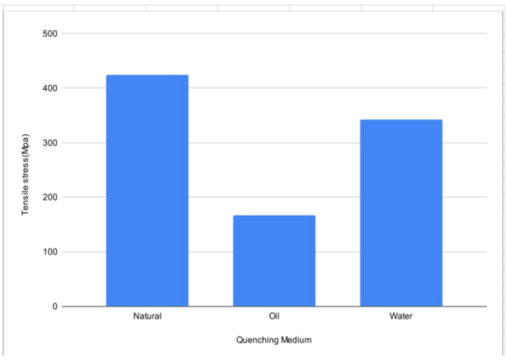

Figure 5: Tensile strength of Gray Cast Iron

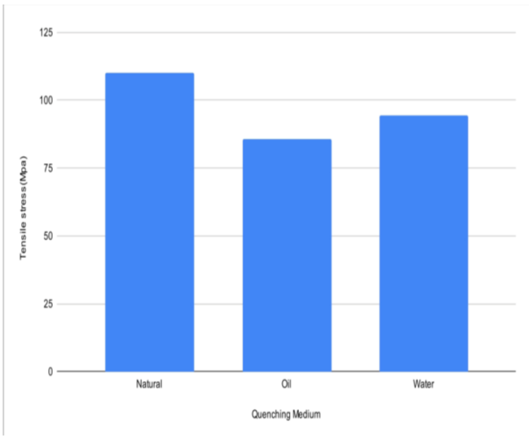

Figure 6: Tensile strength Aluminum Alloy 6063

MICROSTRUCTURAL ANALYSIS AND DISCUSSION

Cast Iron Microstructure

For full rigour, dedicated pre-weld SEM characterisation of both the gray cast iron and Al 6063 base materials would provide an unambiguous baseline for assessing HAZ-induced microstructural changes. In the present study, the naturally cooled base metal micrographs in Figures 7a and 8c serve as the closest available reference to the unaffected material condition.

SEM micrographs in Figure 7 reveal that naturally cooled cast iron exhibits a fine ferrite-pearlite matrix with evenly distributed graphite flakes, consistent with the Class 30 gray iron structure reported by ASM International (2011) and providing the combination of machinability and strength observed in tensile testing. This microstructure is well-documented to result from the slow-cooling eutectoid transformation of austenite in the presence of silicon, which stabilises graphite over cementite (Porter *et al.*, 2009; Adedeji, 2012).

Oil-quenched specimens show a coarser grain structure with a higher bainite fraction, consistent with the intermediate cooling rate preventing full martensite formation yet suppressing the pearlite transformation (Lippold, 2015). Water-quenched HAZ specimens display a mixed-phase microstructure containing martensite alongside graphite nodules, explaining the peak HAZ hardness (292.0 HV) and simultaneous reduction in impact toughness. These findings are consistent with Gharibshahiyan *et al*. (2011), who observed analogous hardness peaks in water-quenched low-carbon steel HAZ. No brittle white-iron (ledeburite) phase was detected in any specimen, confirming that dilution and heat input remained within acceptable limits as recommended by Kou (2003).

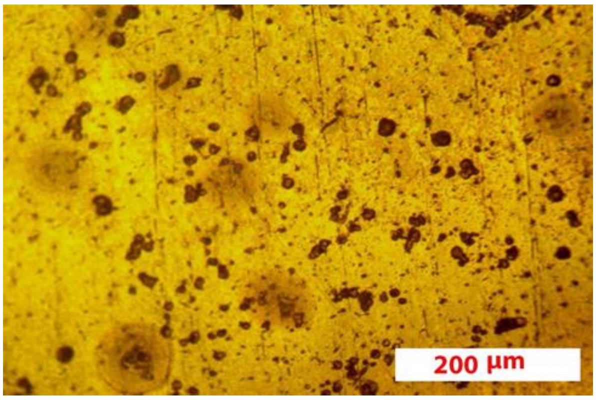

(a) Naturally cooled base metal fine ferrite-pearlite, uniform graphite flakes

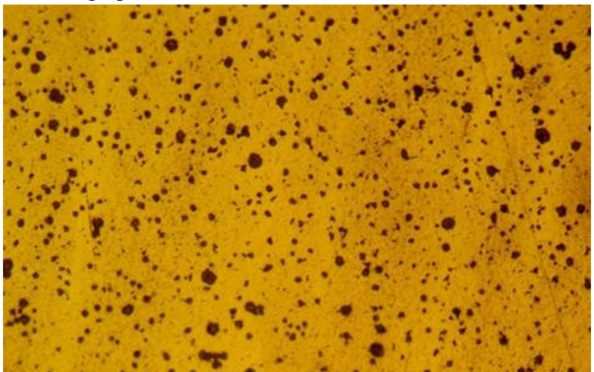

(b) Water-quenched base metal, finer graphite nodules, enhanced hardness

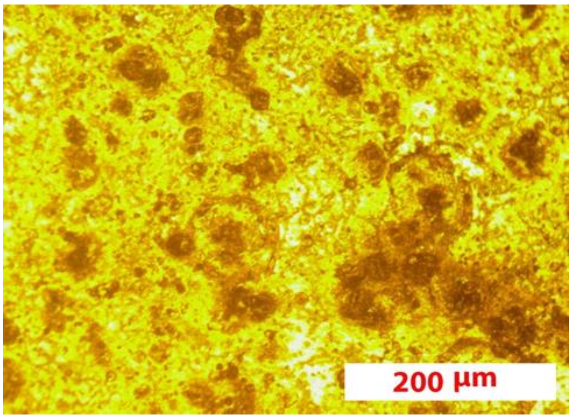

(c) Naturally cooled weldment: bainite matrix, balanced properties

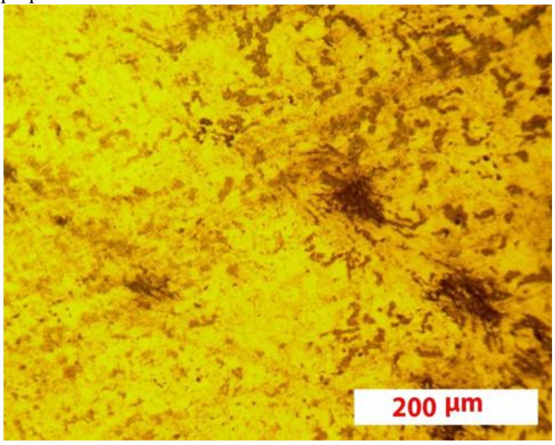

(d) Oil-quenched HAZ - coarse-grained mixed microstructure, peak hardness.

Figure 7: SEM micrographs of Gray Cast Iron-selected zones and conditions

Aluminum Alloy 6063 Microstructure

Although SEM/EDX has confirmed Mg-Si co-enrichment consistent with Mg_2Si in Figure 7a, future XRD analysis would provide full crystallographic confirmation and distinguish this phase from other possible precipitate species such as MgO or Mg_5Si_6 (Callister and Rethwisch, 2018).

SEM/EDX elemental analysis of the fusion interface in Figures 12 and 14 confirmed that no significant Fe-Al interdiffusion was detected in either the cast iron or Al 6063 HAZ regions under the welding parameters employed. While Fe-Al intermetallic phases such as Fe_2Al_5 and $FeAl_3$ are commonly reported in iron-aluminium dissimilar joints (Ekrami *et al*., 2024), they were not identified as a dominant feature in the present specimens. The EDX spectra showed no characteristic Fe-Al stoichiometry at the bond line, suggesting that the combination of welding parameters and joint geometry kept any interfacial reaction layer growth below detectable limits.

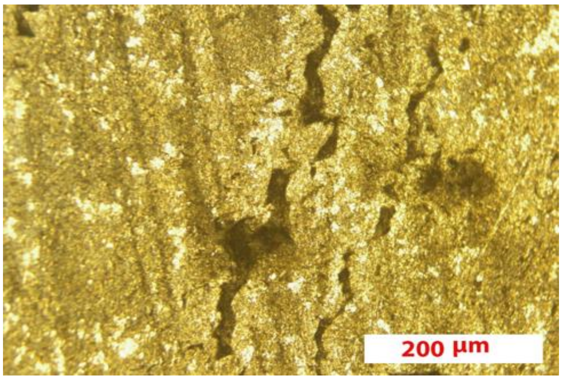

(a) Naturally cooled weldment - coarse-grained, dislocation networks visible.

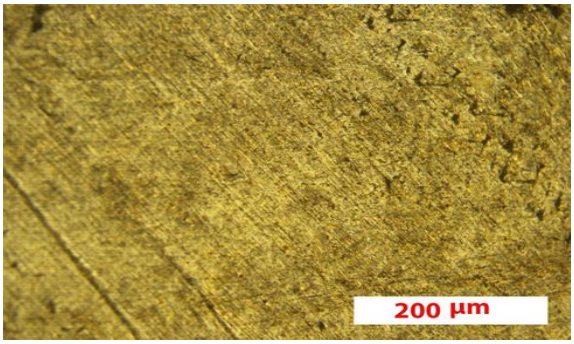

(b) Oil-quenched weldment: dispersed Mg_2Si precipitates, peak hardness

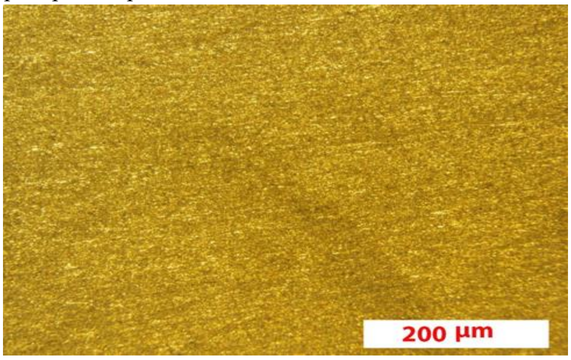

(c) Naturally cooled base metal fine equiaxed grains.

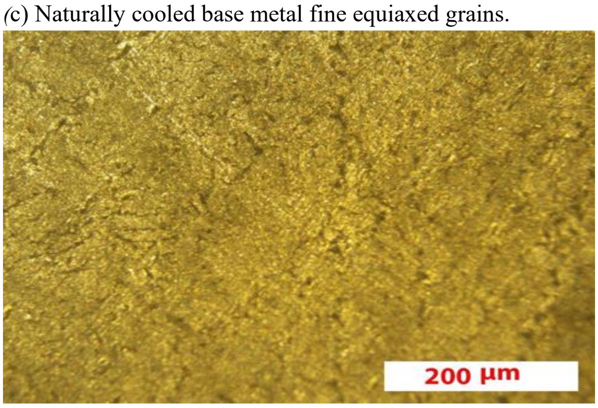

(d) Water-quenched HAZ: finest grain size, dense precipitate distribution

Figure 8: SEM micrographs of Aluminum Alloy 6063 - selected zones and conditions

Cast Iron SEM Analysis

SEM images of the gray cast iron HAZ (200 µm) after natural cooling, water quenching and oil quenching are shown in Figures 9(a), 9(b) and 9(c), respectively. With natural cooling in Figure 9a, the microstructure shows a dark- and light-contrast typical of the ferrite-pearlite matrix and dispersed graphite inclusions found in Class 30 gray iron. The even distribution of dark graphite-rich regions indicates that natural cooling permitted the eutectoid transformation to nearly go to completion, resulting in the equilibrium microstructure that explains the superior tensile strength of 424.5 MPa and impact toughness in this condition (ASM International, 2011; Porter *et al*., 2009). With water quenching in Figure 9b, the faster cooling rate is evident in the pronounced grain boundary features and non-uniform matrix. A large dark crack-like feature dominates the field of view, which is probably a prior austenite grain boundary, and finer and less continuous graphite regions. The relatively fine and uniform matrix texture supports the formation of martensite or bainite, which accounts for the maximum HAZ hardness of 292.0 HV and the decline in impact toughness. The oil-quenched micrograph in Figure 9c occupies an intermediate position: graphite flake continuity is partially preserved and the grain structure is coarser than the water-quenched condition, with the matrix exhibiting a predominantly bainitic character that accounts for the peak weldment hardness of 310.7 HV. No white iron (ledeburite) was detected in any specimen, confirming that heat input remained within acceptable limits (Lippold, 2015).

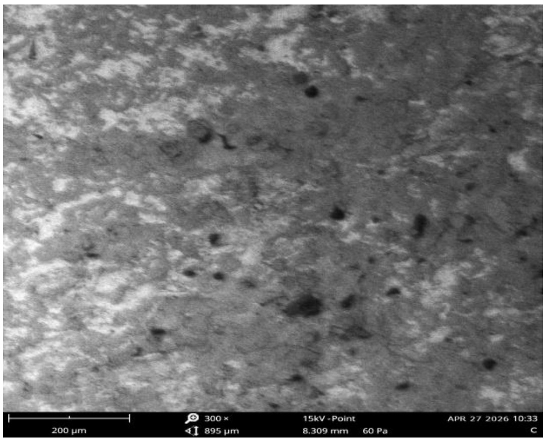

(a) Natural cooling - 200 µm

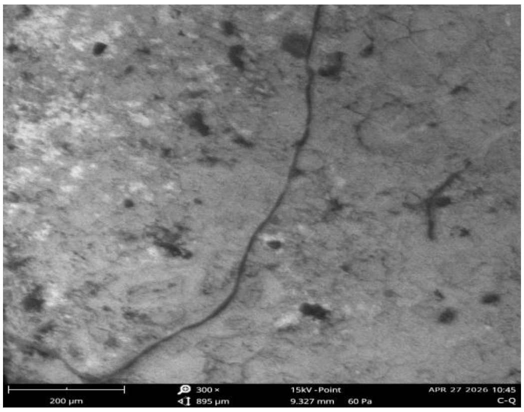

(b) Water quenching - 200 µm

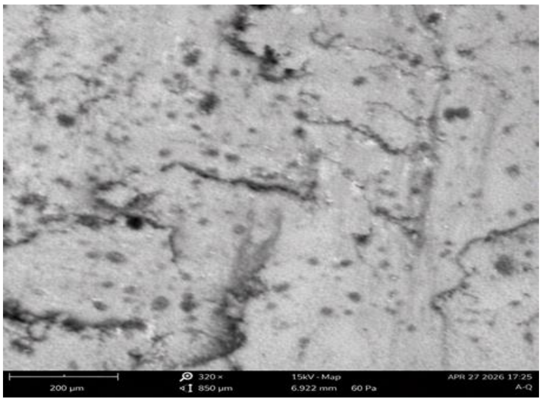

(c) Oil quenching - 200 µm

Figure 9: SEM micrographs of Gray Cast Iron HAZ at 200 µm: (a) natural cooling, (b) water quenching, (c) oil quenching

Aluminum Alloy 6063 SEM Analysis

Figures 10(a), 10(b) and 10(c) present SEM micrographs of the Al 6063 HAZ at 200 µm under natural cooling, water quenching, and oil quenching, respectively. The naturally cooled specimen in Figure 10a presents a predominantly smooth matrix with elongated dark features corresponding to surface relief along grain boundary grooves, consistent with a coarse-grained, well-recovered microstructure in which slow cooling permitted near-complete solid-solution recovery. The sparse dark features are consistent with coarse Mg_2Si particles and this low-dislocation-density microstructure supports the highest tensile strength of 110.2 MPa recorded in this study (Porter *et al*., 2009). The water-quenched micrograph in Figure 10b shows a notably lighter overall contrast with a higher population of small, scattered dark features distributed uniformly across the matrix, consistent with a finer distribution of β" (Mg_2Si) precipitates formed when rapid cooling retains a supersaturated solid solution that partially decomposes via short-range diffusion (Callister and Rethwisch, 2018). Visible surface cracking confirms the presence of residual stresses from rapid thermal contraction, explaining the elevated hardness of 123.3 HV alongside the reduction in impact toughness. The oil-quenched micrograph in Figure 10c shows a partially recovered microstructure with elongated grains, visible sub-grain boundaries, and a finely dispersed, uniform precipitate distribution, consistent with oil quenching achieving the intermediate cooling rate closest to the artificial ageing window for Al 6063. This promotes the maximum density of coherent β" (Mg_2Si) precipitates before coarsening occurs, analogous to artificial peak-ageing (T6 treatment), underpinning the peak weldment hardness of 146.8 HV (Callister and Rethwisch, 2018).

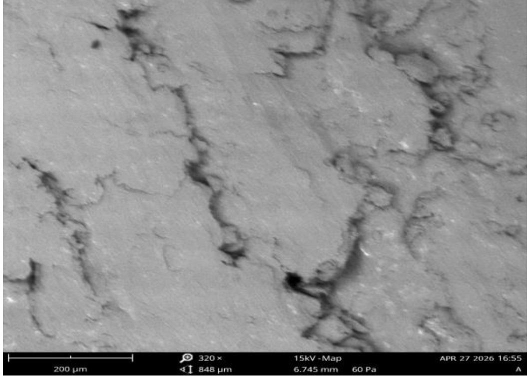

(a) Natural cooling - 200 µm

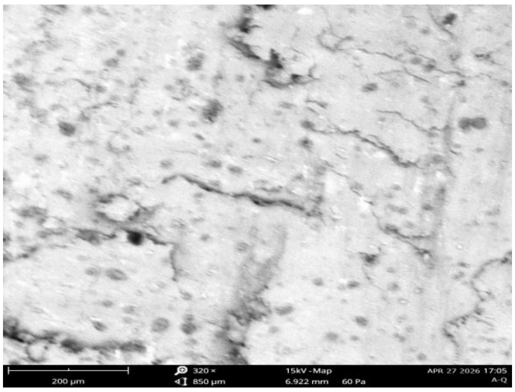

(b) Water quenching - 200 µm

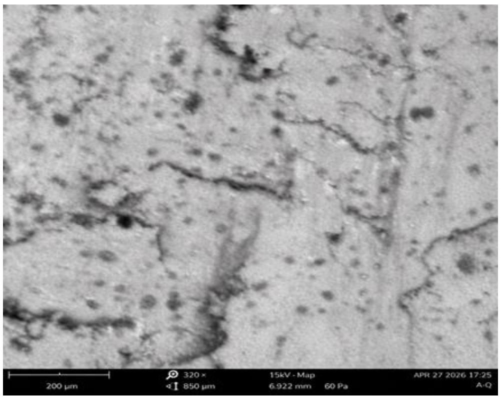

(c) Oil quenching - 200 µm

Figure 10: SEM micrographs of Al 6063 HAZ at 200 µm: (a) natural cooling, (b) water quenching, (c) oil quenching

Mild Steel SEM Analysis

Figures 11(a), 11(b) and 11(c) present SEM micrographs of the mild steel HAZ at 200 µm under natural cooling, water quenching, and oil quenching, respectively. Under natural cooling Figure 11a, the microstructure shows a relatively uniform matrix with a moderate population of dark inclusions and pores, with the ferritic matrix and pearlite colonies evenly distributed, indicating a well-equilibrated ferrite-pearlite microstructure consistent with the moderate hardness and reasonable toughness of naturally cooled mild steel weldments (Porter *et al*., 2009). The water-quenched specimen in Figure 11b exhibits a noticeably finer and more mottled texture, with dark inclusion features appearing smaller and more uniformly dispersed. The refined distribution reflects the reduced time for diffusion-controlled phase separation under rapid cooling, consistent with the CCT behaviour of low-carbon steel where fast cooling promotes bainitic or martensitic structures at the expense of coarser equilibrium ferrite-pearlite products, directly accounting for the elevated HAZ hardness (Porter *et al*., 2009). The oil-quenched micrograph in Figure 11c reveals a mixed microstructure with regions of residual pearlite interspersed with finer bainitic areas, consistent with the intermediate cooling rate placing the transformation predominantly in the bainite temperature range of the CCT diagram (400-550 °C). The absence of significant martensite reflects the low hardenability of mild steel and explains why oil quenching raises weldment hardness without the severe toughness reduction observed in cast iron under the same treatment.

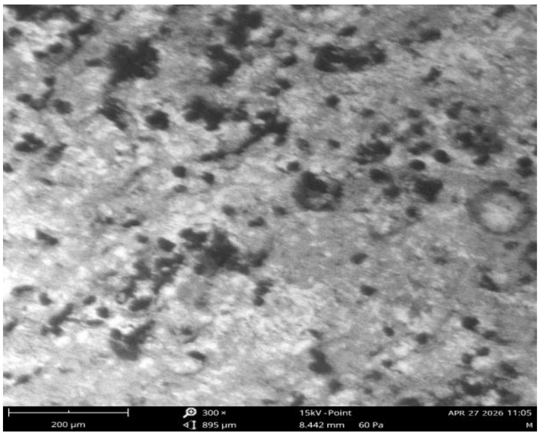

(a) Natural cooling - 200 µm

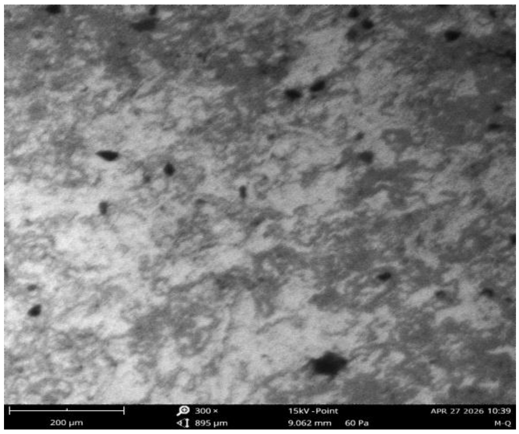

(b) Water quenching - 200 µm

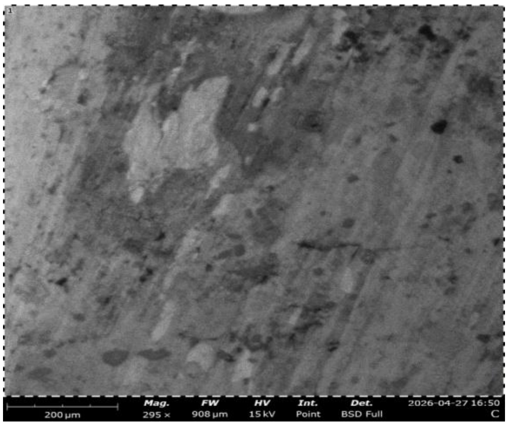

(c) Oil quenching - 200 µm

Figure 11: SEM micrographs of Mild Steel HAZ at 200 µm: (a) natural cooling, (b) water quenching, (c) oil quenching

SEM/EDX Elemental Analysis

The SEM/EDX elemental analysis is presented in three groups corresponding to the three materials investigated. Within each group, the natural cooling, water-quenched, and oil-quenched conditions are presented together as (a), (b), and (c), respectively, allowing direct comparison of the elemental effects of each cooling condition.

Gray Cast Iron EDX Analysis

Figures 12(a), 12(b) and 12(c) present the SEM/EDX elemental maps and spectra for the naturally cooled, water-quenched, and oil-quenched gray cast iron, respectively. In the naturally cooled specimen in Figure 12a, the dominant peaks correspond to Fe with secondary contributions from C and Si, consistent with the ferrite-pearlite-graphite composite microstructure of gray cast iron. The carbon signal appears enriched in the graphite flake regions, confirming the graphitic phase identification made from morphological SEM observation, while the silicon distribution is uniform, consistent with its role as a graphite stabiliser dissolved in the ferritic matrix (ASM International, 2011). No significant aluminium signal was detected, confirming that inter-diffusion of Al across the fusion interface did not extend into the cast iron HAZ under the welding conditions used. In the water-quenched specimen of Figure 12b, the bulk elemental composition is essentially unchanged, as expected from a diffusionless transformation process. The key distinction is that the carbon distribution appears more homogeneous, consistent with carbon being partially trapped in solid solution within the martensitic phase rather than segregated into discrete graphite flakes, providing direct elemental evidence for the martensitic transformation inferred from hardness data. In the oil-quenched specimen in Figure 12c, the carbon signal distribution reflects partial homogenisation consistent with bainitic matrix formation, in which carbon is redistributed from graphite flakes into the surrounding matrix. Silicon remains uniformly distributed and no aluminium signal is detected, confirming that the elevated hardness of 310.7 HV is entirely attributable to the bainitic microstructural transformation rather than any chemical contamination.

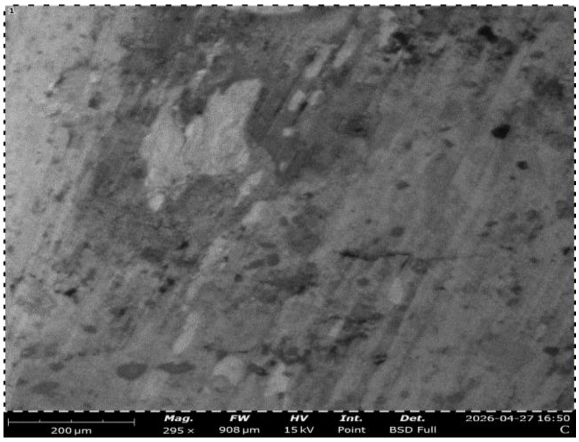

(a) Natural cooling - EDX elemental map

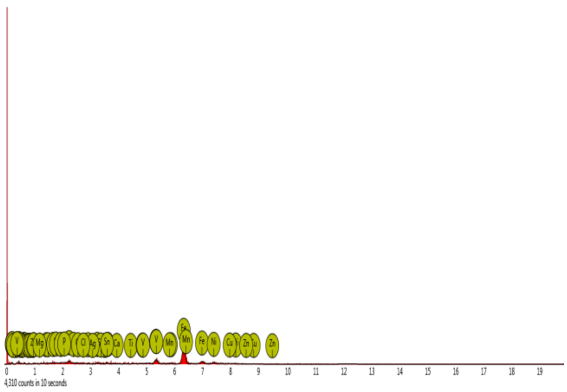

(a) Natural cooling - EDX spectrum

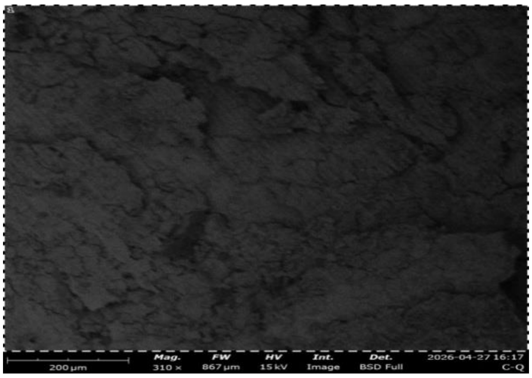

(b) Water quenching - EDX elemental map

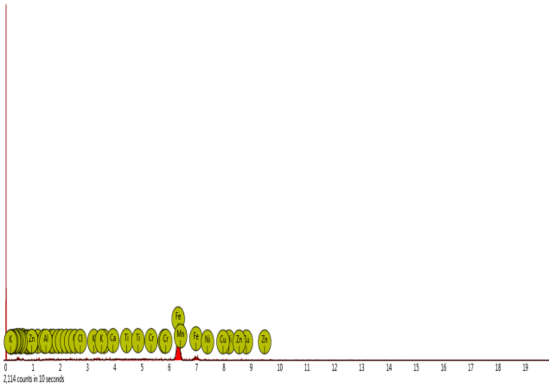

(b) Water quenching - EDX spectrum

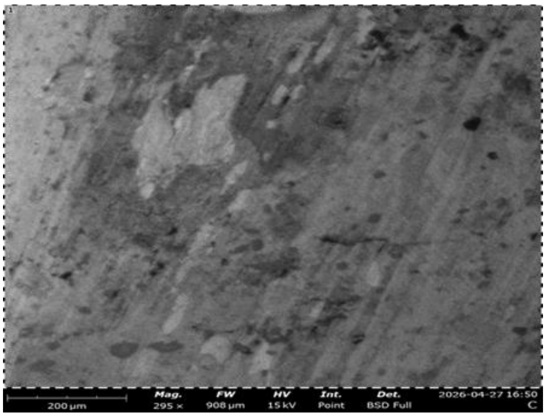

(c) Oil quenching - EDX elemental map

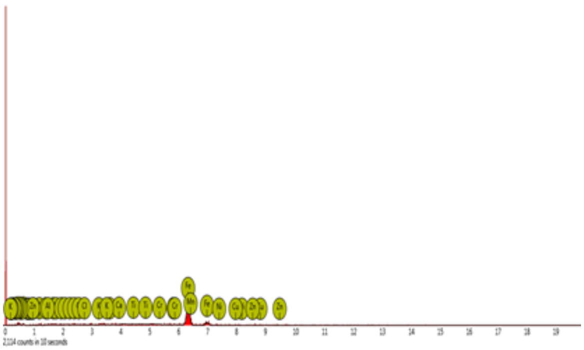

(c) Oil quenching - EDX spectrum

Figure 12: SEM/EDX analysis of Gray Cast Iron: (a) natural cooling, (b) water quenching, (c) oil quenching

Aluminum Alloy 6063 EDX Analysis

Figures 13(a), 13(b) and 13(c) present the SEM/EDX analysis of Al 6063 under natural cooling, water quenching, and oil quenching, respectively. In the naturally cooled condition of Figure 13a, the EDX map confirms regions of Mg and Si co-enrichment at grain boundaries and within grains at locations corresponding to the precipitate features identified in the SEM micrographs. The co-localisation of Mg and Si in approximately a 2:1 atomic ratio is consistent with the stoichiometry of Mg_2Si, providing direct elemental evidence for the precipitation of this strengthening phase (Callister and Rethwisch, 2018). The water-quenched EDX of Figure 13b shows a higher number density of smaller Mg-Si-enriched regions compared to the naturally cooled condition, consistent with the finer precipitate distribution observed in the SEM micrograph. The spectrum confirms similar elemental proportions, demonstrating that the bulk composition is unchanged and that the hardness increase under quenching arises from a denser population of fine Mg_2Si precipitates providing more effective dislocation barrier strengthening. The oil-quenched EDX of Figure 13c reveals the highest spatial density of Mg-Si co-enriched zones of all three conditions, consistent with the finest and most uniform Mg_2Si precipitate distribution produced at a cooling rate closest to the artificial ageing window for this alloy, directly explaining the peak weldment hardness of 146.8 HV. The Mg and Si signals are present in approximately a 2:1 atomic ratio across all three conditions and the aluminium matrix signal confirms the absence of significant Fe-Al interdiffusion at the fusion interface.

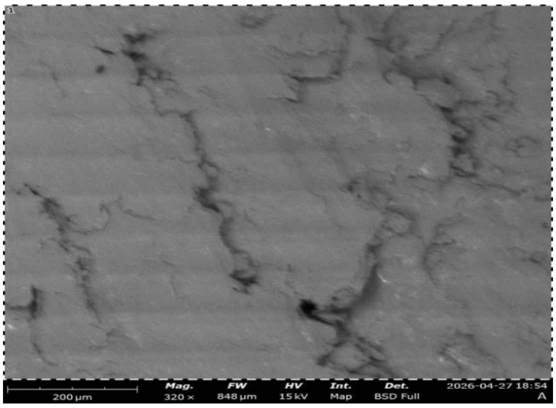

(a) Natural cooling - EDX elemental map

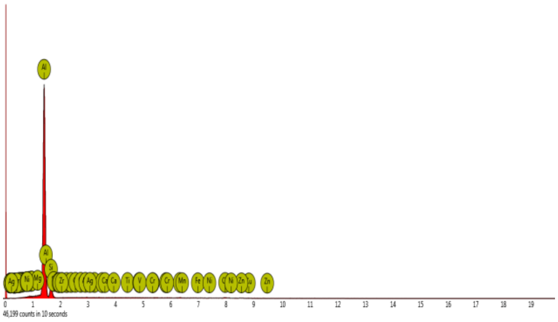

(a) Natural cooling - EDX spectrum

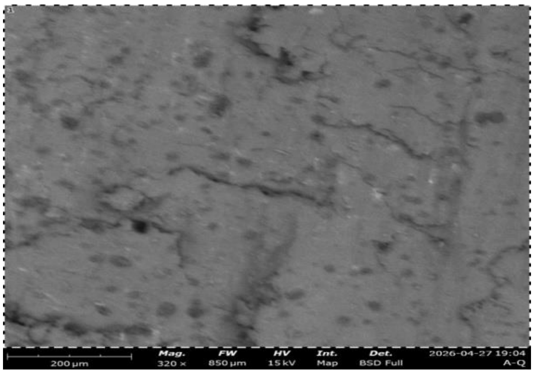

(b) Water quenching - EDX elemental map

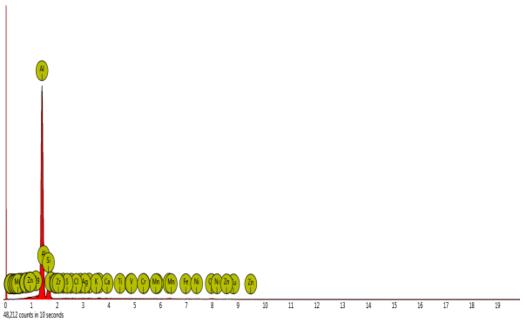

(b) Water quenching - EDX spectrum

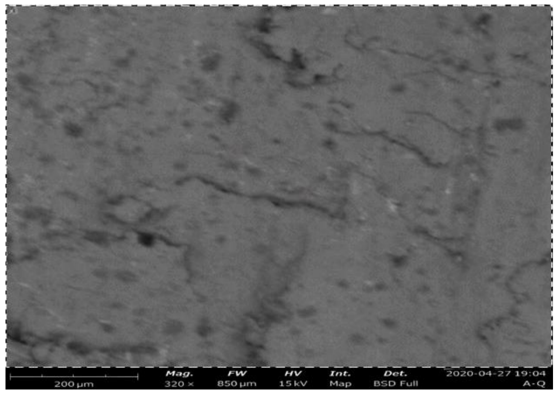

(c) Oil quenching - EDX elemental map

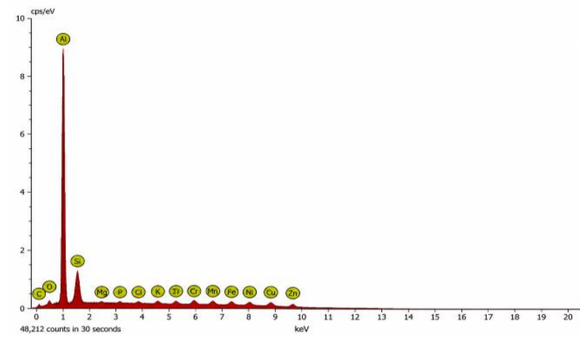

(c) Oil quenching - EDX spectrum

Figure 13: SEM/EDX analysis of Aluminum Alloy 6063: (a) natural cooling, (b) water quenching, (c) oil quenching

Mild Steel EDX Analysis

Figures 14(a), 14(b) and 14(c) present the SEM/EDX analysis of mild steel under natural cooling, water quenching, and oil quenching, respectively. In all three conditions, the EDX maps and spectra confirm that the mild steel composition is dominated by Fe with minor contributions from C and Mn, consistent with low-carbon steel. No significant aluminium signal was detected in any of the three conditions, confirming that the welding parameters limited Fe-Al interdiffusion to within the fusion zone and that the mechanical property changes in the mild steel HAZ are attributable entirely to microstructural transformation. In the naturally cooled specimen of Figure 14a, the carbon distribution is heterogeneous, reflecting its segregation into discrete pearlite colonies within the ferritic matrix. In the water-quenched specimen of Figure 14b, the carbon distribution appears more homogeneous, consistent with partial trapping of carbon in bainitic or martensitic phases rather than its full segregation into coarse pearlite. The oil-quenched specimen in Figure 14c shows a carbon distribution intermediate between the two extremes, consistent with the bainitic transformation that characterises this cooling condition and accounts for the intermediate hardness measured in the mild steel weldment. Taken together, the EDX results across all three materials confirm that cooling rate governs microstructural phase transformation rather than bulk elemental composition, and that no significant Fe-Al intermetallic compounds were detected at the fusion interface across all conditions examined (Ekrami *et al*., 2024).

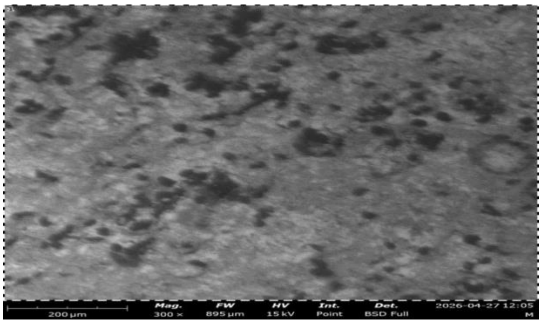

(a) Natural cooling - EDX elemental map

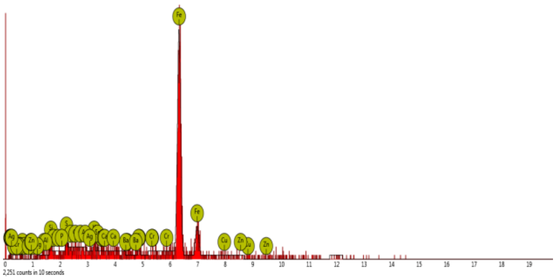

(a) Natural cooling - EDX spectrum

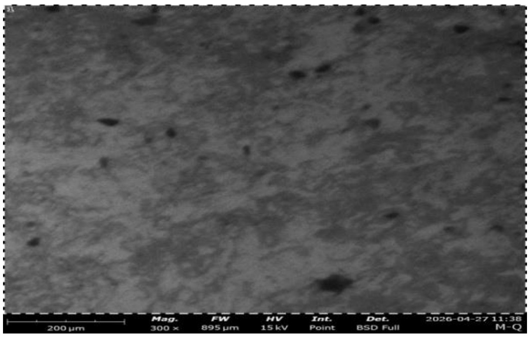

(b) Water quenching - EDX elemental map

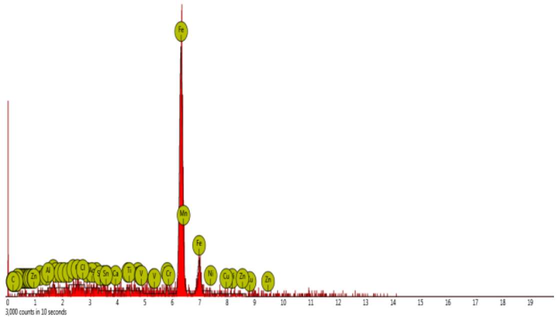

(b) Water quenching - EDX spectrum

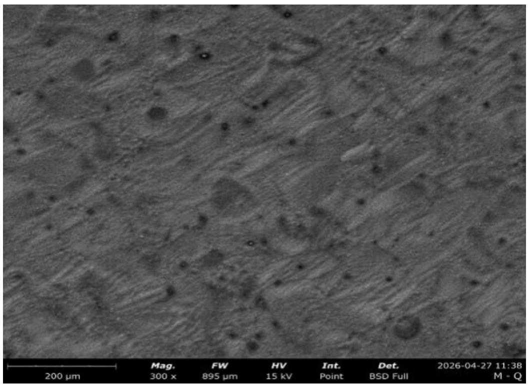

(c) Oil quenching - EDX elemental map

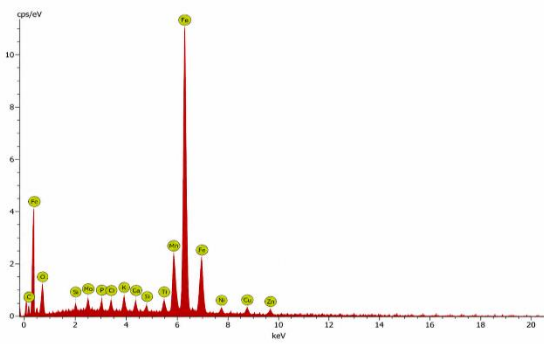

(c) Oil quenching - EDX spectrum

Figure 14: SEM/EDX analysis of Mild Steel: (a) natural cooling, (b) water quenching, (c) oil quenching

Property-Microstructure Correlations

The mechanical property-microstructure correlations that are observed are internally consistent in both materials and are consistent with the existing theory (Porter *et al*., 2009; Callister and Rethwisch, 2018). Hardness proportional to the martensite/bainite fraction and precipitate density, which are directly proportional to the cooling rate. This is the Hall-Petch relationship that is expected: smaller microstructural constituents hinder dislocation movement, increasing hardness and yield strength (Lippold, 2015). Impact toughness is the opposite: fast quenching favors harder and more brittle phases, which hinder plastic deformation before a crack propagates, eliminating absorbed energy (Lancaster, 1999). The continuity and morphology of the graphite network is the predominant tensile strength factor in cast iron; rapid quenching destroys this network and leaves residual stresses that act as ready cracks nucleation sites which has been observed to result in the apparent paradox of greater hardness but lower UTS under rapid cooling, a phenomenon previously observed by Adedeji (2012) and is also consistent with the presence of the brittle fracture modeThe lower UTS range (85.8-110.2 MPa) of aluminum alloy is a consequence of the higher ductile nature of the fcc matrix compared to cast iron, and the relative ranking of the cooling conditions by UTS is similar to that of 6xxx-series alloys reported by Balasubramanian *et al*. (2008) and Wang *et al*. (2023). All these findings demonstrate that in this non-similar couple, no single cooling method can be used to optimise all mechanical properties. The quenching medium selected should thus depend on the predominant service need: hardness and wear resistance (oil quenching), or toughness and tensile load-bearing capacity (natural cooling). This result is a reflection of the overall rule by Messler (2004) and Kou (2003) that the thermal management of the post-weld is as important as the actual welding process in the performance of the joint.

CONCLUSION

Post-weld cooling strategy was found to exert a decisive influence on both the microstructure and mechanical properties of TIG-welded Gray Cast Iron / Aluminum Alloy 6063 dissimilar joints. Oil quenching maximised weldment hardness in both materials (310.7 HV in cast iron; 146.8 HV in Al 6063), while water quenching produced the highest HAZ hardness in cast iron (292.0 HV). Natural cooling consistently preserved the highest tensile strength and impact toughness across all zones, with cast iron reaching 424.5 MPa, a value 2.5 times that of the oil-quenched condition, attributed to the brittle martensite and residual stresses that form under rapid cooling. SEM analysis confirmed water quenching produced martensitic lath structures in the cast iron HAZ, oil quenching produced a bainitic matrix, and natural cooling preserved the equilibrium ferrite-pearlite-graphite microstructure, consistent with classical CCT behaviour and confirming that the TIG welding temperature at 240 V and 90 A was sufficient to austenitise the HAZ. SEM/EDX analysis confirmed Mg and Si co-enrichment in approximately a 2:1 atomic ratio in Al 6063 precipitate regions, providing direct elemental evidence for Mg_2Si as the primary strengthening phase, with oil quenching producing the highest precipitate density consistent with its peak hardness. Mild steel HAZ evolution followed the same cooling-rate-governed pattern as cast iron. No significant Fe-Al interdiffusion was detected at the fusion interface under any cooling condition, indicating that any intermetallic reaction layer remained below detectable limits. No single cooling strategy optimises all properties simultaneously: oil quenching is preferred for wear-critical applications, while natural cooling is recommended for structural applications requiring high tensile strength and toughness. Future work should include XRD for crystallographic phase confirmation, pre-weld SEM baseline characterisation, and SEM/EDX line scans across the fusion interface to quantitatively map Fe-Al elemental gradients.

REFERENCES

Adedeji, A. S. (2012). Effects of heat treatment on the mechanical properties of cast iron. International *Journal of Engineering Research and Applications*, 2(4), 1033-1040.

Adedeji, A. S., Oguntuase, A. M. and Akinlabi, E. T. (2018). Mechanical and microstructural properties of TIG-welded dissimilar metals. *Materials Science Forum,* 928, 112-120.

ASM International (2011). ASM Handbook, Volume 4: Heat Treating. ASM International, Materials Park, Ohio, USA.

Baghel, P. K. (2022). Effect of SMAW process parameters on similar and dissimilar metal welds: an overview. *Heliyon*, 8(12), e12161. https://doi.org/10.1016/j.heliyon.2022.e12161

Balasubramanian, V., Ravisankar, V. and Madhusudhan Reddy, G. (2008). Effect of pulsed current welding on mechanical properties of high-strength aluminum alloy. *International Journal of Advanced Manufacturing Technology*, 36, 254-262.

Callister, W. D. and Rethwisch, D. G. (2018). Materials Science and Engineering: An Introduction, 10th ed. John Wiley and Sons, New York, USA.

Cao, X., Zhang, Q., Yu, J., and Yu, X. (2025). Effect of compositional changes and heat treatment on microstructure and mechanical properties of gray cast iron. *Journal of Materials Research and Technology*, 35, 5336-5352. https://doi.org/10.1016/j.jmrt.2025.02.166

Cui, S., Yu, Y., Ma, R., Tian, F. and Pang, S. (2023). Study on morphology, microstructure and properties of 6063-T6 aluminum alloy joints in MIG welding. *Materials*, 16(13), 4886. https://doi.org/10.3390/ma16134886

Ekrami, O., Khodabakhshi, F. and Gerlich, A. P. (2024). Study on intermetallic compound (IMC) in dissimilar joining of steel and aluminum (Fe-Al): a review paper. *Welding in the World*, 68, 2127-2168. https://doi.org/10.1007/s40194-024-01784-8

Gharibshahiyan, E., Raouf, A. H., Parvin, N. and Rahimian, M. (2011). The effect of microstructure on hardness and toughness of low-carbon welded steel using inert gas welding. *Materials and Design*, 32, 2042-2048. https://doi.org/10.1016/j.matdes.2010.11.056

ISO 148-1 (2016). Metallic Materials Charpy Pendulum Impact Test Part 1: Test Method. International Organization for Standardization, Geneva, Switzerland.

ISO 6507-1 (2018). Metallic Materials Vickers Hardness Test Part 1: Test Method. International Organization for Standardization, Geneva, Switzerland.

Kou, S. (2003). Welding Metallurgy, 2nd ed. John Wiley and Sons, Hoboken, New Jersey, USA.

Lancaster, J. F. (1999). Metallurgy of Welding, 6th ed. Abington Publishing, Cambridge, UK.

Lippold, J. C. (2015). Welding Metallurgy and Weldability. John Wiley and Sons, Hoboken, New Jersey, USA.

Messler, R. W. (2004). Principles of Welding: Processes, Physics, Chemistry and Metallurgy. Wiley-VCH, Weinheim, Germany.

Ning, H., Li, X., Meng, L., Jiang, A., Ya, B., Ji, S., Zhang, W., Du, J. and Zhang, X. (2023). Effect of Ni and Mo on microstructure and mechanical properties of grey cast iron. *Materials Technology*, 38(1), 2172991. https://doi.org/10.1080/10667857.2023.2172991

Okafor, E. C., Okolie, J. A. and Ezeh, J. I. (2022). Microstructural and mechanical characterisation of TIG-welded dissimilar aluminum alloy joints for automotive applications. *International Journal of Advanced Manufacturing Technology*, 119, 3411-3424.

Porter, D. A., Easterling, K. E. and Sherif, M. Y. (2009). Phase Transformations in Metals and Alloys, 3rd ed. CRC Press, Boca Raton, Florida, USA.

Ramji, B. R., Bharathi, V., and Prabhu Swamy, N. R. (2021). Characterisation of TIG and MIG welded aluminum 6063 alloy. Materials Today: Proceedings, 46, 8895-8899. https://doi.org/10.1016/j.matpr.2021.05.356

Wang, J., Chen, M. and Li, Y. (2023). Effect of alloying elements on intermetallic formation during friction stir welding of dissimilar metals: a critical review on aluminum/steel. *Metals*, 13(4), 768. https://doi.org/10.3390/met13040768

Zhang, W., Gao, H., Liu, D., Gao, Y., Zhang, Y. and Kong, L. (2024). Effects of heat treatment on microstructures and mechanical properties of a low-alloy cylinder liner. *Materials*, 17(4), 802. https://doi.org/10.3390/ma17040802